Restricted diffusion preparation of fully-exposed Fe single-atom catalyst on carbon nanospheres for efficient oxygen reduction reaction

Libo Deng [a],[*], Lei Qiu [a], Rong Hu [a], Lei Yao [b],[*], Zijian Zheng [c], Xiangzhong Ren [a], Yongliang Li [a], Chuanxin He [a],[*]

[a] College of Chemistry and Environmental Engineering, Shenzhen University, Shenzhen 518060, China
[b] Shenzhen Key Laboratory of Special Functional Materials, Shenzhen Engineering Laboratory for Advanced Technology of Ceramics, Guangdong Research Center for Interfacial Engineering of Functional Materials, College of Materials Science and Engineering, Shenzhen University, Shenzhen 518060, China
[c] Institute of Textiles and Clothing, and Research Institute for Smart Energy, The Hong Kong Polytechnic University, Hong Kong, China

ABSTRACT

Single-atom catalysts (SAC) stabilized by nitrogen in carbon support are promising candidates for oxygen reduction reaction (ORR). However, conventional preparation methods usually lead to encapsulation of metallic centers in matrix and thus the utilization efficiency (UE) is underexploited. Herein, we report a novel strategy to prepare an Fe-SAC with all Fe atoms anchored on the surface of carbon nanospheres, which exhibited an extraordinary UE of 80% for ORR. This efficiency was achieved by coating polydopamine spheres with silica, followed by the pyrolysis of their blend with $FeCl_3$. During thermal treatment, Fe migrates across the silica shell by atomic exchange with silicon, which inhibits the aggregation of Fe and allows Fe atoms to anchor on the surface. As such, it showed excellent ORR activity at a low Fe content. Zn-air batteries assembled using this catalyst showed a peak power density of 113 mW cm^{-2} and specific capacity of 710 mAh g$_{Zn}^{-1}$.

1. Introduction

Recently, carbon-supported single-atom catalysts (SACs) stabilized by nitrogen (M-N-C) have attracted increasing interest as promising candidates to replace the benchmark Pt-based catalysts for the oxygen reduction reactions (ORR) [1,2]. This interest is associated with the full theoretical utilization of their catalytic active centers and the various coordination environments that impart intriguing electronic structures to the metallic center, which distinguishes them from nanoparticles. Furthermore, this interest is also related to practical aspects such as the abundance and low cost of non-precious metals, as well as their excellent catalytic performance in both alkaline and acidic media (such as Fe-based catalysts) [1–5]. In addition to improving their intrinsic activity, extensive efforts have been devoted to increase the content of single-atomic metallic species in these catalysts, aiming for a larger number of active sites and hence, a better catalytic performance. Many strategies with coherent mechanisms, such as spatial confinement [6], coordination site construction [7] and defect capturing [8], have been developed to ensure the formation of single atoms (instead of particles) on the carbon support, and SACs with up to 16 wt% of atomic metal have

been reported recently [9–11].

However, not all single-atomic sites in carbon-supported SACs contribute to the ORR activity [12,13]. Generally, the atomic M–N$_x$ moieties at the outer surface of the catalysts are better able to participate in the ORR, whereas those blocked by dense graphitic domains or water flooding in micropores remain inactive [14–17]. So far, the utilization efficiency (UE) of these atomic sites, namely the effective sites contributing to ORR among the total metallic elements in SACs, has been unsatisfactory. For instance, the UE is only 4.5% for the classic carbon black derived Fe-SAC [18], 43% for zeolitic imidazolate framework (ZIF)-derived concave Fe-SAC [17], 10% for Fe-SAC from fumed silica templates [19], 22.3% for Co-SAC anchored on carbon nanosheets [20], and ~7.6% for ZIF-derived Co-SAC [21]. The presence of inaccessible atomic species in carbon not only wastes the metallic resources (cost becomes more obsessed when relying on precious metallic sites), but also induces inhomogeneity and instability. Therefore, the development of better preparation methods and reliable techniques to quantify the active sites are crucial for increasing the UE of the active sites [22].

Recently, a strategy using silica as a coating material to prevent the pyrolysis of the encapsulated carbon source was found to be particularly

---

effective for preparing M-N-C catalysts with high M-N$_x$ moieties [23–26]. This approach is based on the fact that the SiO$_2$-protected shells can facilitate the reaction of nitrogen atoms with metallic atoms to form more active M-N$_4$ species; it can also trap volatile gaseous substances during pyrolysis, which generates a porous structure. Catalysts prepared using this approach have demonstrated impressive catalytic performances in the past few years [24,25]. However, in most cases, this strategy was conducted by impregnating metallic species into carbon sources before silica coating, through which metal atoms can freely penetrate into the interior region, and the atomic sites are mostly embedded in the dense carbon matrix. The highest UE for SAC prepared by silica-confined pyrolysis so far, derived from silica-coated ZIF, is ~43%, yet the UE decreases rapidly with the increase of the metallic content [17].

Herein, unlike the conventional silica-confined pyrolysis approach in which metallic species are introduced into the carbon source freely prior to carbonization, we employed a silica-restricted diffusion strategy to prepare an Fe-N-C catalyst with single Fe atoms anchored on the outermost surface of the carbon nanosphere (CNS). This was achieved by first coating the polydopamine nanospheres (PDAS) with a thin silica layer. The core-shell composites were physically mixed with FeCl$_3$, followed by pyrolysis and the removal of the silica shell. In this process, the Fe atoms were introduced by diffusing across the silica layer, and thus, the aggregation of Fe in the carbon matrix is intrinsically restricted at the atomic level; more importantly, the diffusion through the silica shell allows for the Fe species to reach only the surface underneath the CNS, enabling the complete exposure of the active sites. This catalyst exhibited a high activity toward ORR in both alkaline and acidic electrolytes, requiring an extremely low loading of Fe.

2. Experimental

2.1. Materials

Dopamine hydrochloride (C$_8$H$_{11}$NO$_2$•HCl, 98%), anhydrous ferric chloride (FeCl$_3$), ammonia solution (NH$_3$·H$_2$O, 25–28%), tetraethyl orthosilicate (C$_8$H$_{20}$O$_4$Si, TEOS), absolute ethanol (C$_2$H$_6$O, 99.5%), hydrochloric acid (HCl, ~37%), potassium hydroxide (KOH, 95%), and perchloric acid (HClO$_4$, 70%) were purchased from Shanghai Aladdin Biochemical Technology Co., Ltd. A commercial Pt/C catalyst (20 wt%) was purchased from the Johnson Matthey Corporation. A 5 wt% Nafion solution was purchased from DuPont Corporation.

2.2. Synthesis of PDAS

Ammonia solution (0.8 mL) was added to a solution containing 90 mL of deionized water and 40 mL of absolute ethanol. The resultant solution was stirred for 10 min. Subsequently, 10 mL of a dopamine hydrochloride solution (5 wt%) was added, and the mixture was stirred at 23 °C for 30 h. During this process, the color of the solution changed from pink to light brown and finally to dark brown. PDAS was then obtained by centrifugation and washed three times with deionized water and absolute ethanol.

2.3. Coating of PDAS with silica (PDAS@SiO$_2$)

PDAS (100 mg) was added to a mixed solution of 100 mL deionized water and 10 mL absolute ethanol and sonicated for 20 min, followed by the addition of 1.5 mL ammonia solution and stirring for 10 min. TEOS (2 mL) was then added dropwise to the dispersed solution and stirred at room temperature for 12 h. After the reaction, PDAS@SiO$_2$ was collected by centrifugation and washed thoroughly with absolute ethanol and deionized water.

2.4. Synthesis of the electrocatalysts

The electrocatalysts were prepared using the following process: 100 mg of PDAS@SiO$_2$ was dispersed in 10 mL of deionized water containing 100 mg of anhydrous FeCl$_3$. The resultant mixture was sonicated for 30 min and dried at 65 °C overnight to form a uniform blend. The dried product was heated at 400 °C for 1 h and subsequently at 800 °C for 2 h under Ar atmosphere at a heating rate of 5 °C min^{-1}. The pyrolytic black powder was leached using 2 M HCl for 30 min to remove the Fe-containing particles on the surface. The powder was then soaked in a 3 M KOH solution and stirred for 24 h to remove the silica shell. The etched product was heated again at 800 °C for 1 h to produce the final product. As the Fe source was adsorbed on the outer silica layer, the final catalyst was denoted as OAC.

For comparison, two other types of precursors were also used for carbonization: (1) FeCl$_3$ was first adsorbed onto PDAS and then coated with SiO$_2$. Specifically, 100 mg of PDAS were dispersed in 10 mL of deionized water containing 100 mg of anhydrous FeCl$_3$. The resultant solution was sonicated for 30 min and subsequently filtered. This step resulted in an Fe content of 1.5 wt% in the PDAS. The impregnated nanospheres were then coated with silica and carbonized at 800 °C for 2 h. The pyrolytic product was then soaked in a 3 M KOH solution and stirred for 24 h to remove the silica shell, followed by acid leaching in 2 M HCl for 12 h to remove the Fe-containing particles. (2) FeCl$_3$ was adsorbed into the PDAS and used as the precursor directly without the SiO$_2$ coating. The subsequent carbonization procedure was the same as that used for OAC. These two products are denoted as IAC (which was produced by the adsorption of FeCl$_3$ inside the silica layer) and UCC (which represents the uncoated carbonization), respectively.

2.5. Material characterization

Field-emission scanning electron microscopy (FE-SEM) was performed on a JEOL JSM-7800 F. Transmission electron microscopy (TEM) images were acquired on a JEM-2100. Aberration-corrected high-resolution scanning transmission electron microscopy (STEM) was conducted with a Titan Cubed Themis G2 300. X-ray diffraction (XRD) characterization was carried out on a Bruker/D8 Advance instrument equipped with Cu Kα radiation. Raman spectroscopy was performed on a Renishaw/INVIA REFLEX spectrometer coupled with a 633 nm laser. N$_2$ adsorption-desorption isotherm test was performed on a Micromeritics ASAP 2460 instrument. X-ray photoelectron spectroscopy (XPS) measurements were performed on an Ultra DLD using a monochromic Al X-ray source. Inductively coupled plasma optical emission spectrometry (ICP-OES) measurements were performed using an Avio 200 instrument. Mössbauer spectroscopy was performed at room temperature (295 K) using a conventional spectrometer (Wissel MS-500) in transmission geometry and a constant acceleration mode. A ^{57}Co (Rh) source with an activity of 25 mCi was used. Velocity calibration was performed using an α-Fe absorber at room temperature. The spectra were fitted using the Recoil software and Voigt-based fitting (VBF) analysis. The X-ray absorption spectra were collected on beamline BL01C1 at the NSRRC (Taiwan). The radiation was monochromatized using a Si(111) double-crystal monochromator. X-ray absorption near edge structure (XANES) and extended X-ray absorption fine structure (EXAFS) data reduction and analysis were performed using the Athena software.

2.6. Electrochemical measurements

To prepare the working electrode, a catalyst ink was first prepared by dispersing the catalyst (4 mg) and Nafion solution (50 μL) in 2 mL of ethanol and sonicated for 15 min. The catalyst ink was dripped on a rotating disk electrode (RDE) or a rotating ring disk electrode (RRDE) with a certain volume to obtain the desired catalyst loading. Solutions of 0.1 M KOH and 0.1 M HClO$_4$ served as the alkaline and acid electrolytes, respectively. The loading density of the synthesized catalyst in both

electrolytes was 0.3 mg cm^{-2} and that for commercial Pt/C (20 wt%) was 80 µg cm^{-2}.

The catalytic activity was investigated using a CHI 760E electrochemical workstation with a standard three-electrode system at room temperature. A Pt wire and an Ag/AgCl electrode in saturated KCl solution served as the counter and reference electrodes, respectively. The potential was measured against an Ag/AgCl electrode and was converted into a potential (V) versus reversible hydrogen electrode (RHE) according to the following equations: E (vs. RHE) = E (vs. Ag/AgCl) + 0.966 V in 0.1 M KOH and E (vs. RHE) = E (vs. Ag/AgCl) + 0.278 V in 0.1 M HClO$_4$ (the calibration curves in alkaline and acidic electrolyte solutions are shown in Fig. S1 in the Supporting Information). Cyclic voltammograms (CVs) and linear sweep voltammograms (LSVs) were obtained at a sweep rate of 10 mV s^{-1}. For RDE test, the rotation speed was varied from 400 to 2500 rpm. LSV curves acquired in the N$_2$-saturated electrolyte were used as the capacitive background and were subtracted from the working curves under the same testing condition (i. e. the same rotating speed).

2.7. Quantification of the active sites

The number of active sites was determined through the nitrite poisoning test as per the procedure reported in previous studies [17,18]. Briefly, the catalyst deposited on the RDE was first activated by CV measurements in an N$_2$-saturated and subsequently in O$_2$-saturated sodium acetate buffer (pH 5.2). The CV measurements were performed at a scan rate of 10 mV s^{-1} and in the potential range of $-$ 0.4–1.05 V vs RHE. These measurements were repeated several times until the CV curves overlapped. CV curves were then acquired in N$_2$-saturated sodium acetate buffer at a scan rate of 10 mV s^{-1} and in the potential range of $-$ 0.35–0.35 V vs RHE; these curves were denoted as the curves for unpoisoned catalysts. To poison the electrode, it was soaked in a 125 mM NaNO$_2$ solution for 5 min at the open-circuit potential (OCP) with a rotating speed of 300 rpm. Afterwards, the electrode was soaked in deionized water for 1 min at OCP and with a rotating speed of 300 rpm. It was then dipped in a sodium acetate buffer for 5 min at OCP with a rotating speed of 300 rpm, and finally soaked in deionized water again until the complete removal of physically adsorbed NaNO$_2$. CV curves were then acquired in N$_2$-saturated sodium acetate buffer at a scan rate of 10 mV s^{-1} and in the potential range of $-$ 0.35–0.35 V vs RHE; these curves were defined as the curves for the poisoned catalyst. The site density (SD) and turnover frequency (TOF) were calculated using the following equations [18]:

$$SD(mol\ g^{-1}) = \frac{Q_{strip}(C\ g^{-1})}{n_{strip}F(C\ mol^{-1})} \tag{1}$$

$$TOF(S^{-1}) = \frac{n_{strip}\Delta J_k(mA\ cm^{-2})}{Q_{strip}(C\ g^{-1})L_c(mg\ cm^{-2})}, \tag{2}$$

in which $J_k = \frac{j_{lim} \times j}{j_{lim}-j}$,

$$J_k = \frac{j_{lim} \times j}{j_{lim} - j}$$

Here, Q_{strip} is the excess coulometric charge associated with the stripping peak; n_{strip} (= 5) is the number of electrons associated with the reduction of one nitrite per site; F is the Faraday's constant (96,485.3 C mol^{-1}), J_k is the kinetic current, j is the current density at 0.8 V, j_{lim} is the current at 0.3 V, and L_c is the loading of the catalyst.

2.8. Assembly and tests of primary Zn–air batteries

Primary Zn-air batteries were tested in home-built electrochemical cells. Here, catalyst ink deposited on nickel foam was used as the air cathode, a polished zinc plate was used as the anode, and 6 M KOH was used as the electrolyte. To prepare the air cathode, ethanol solution was added to a mixture of the catalyst, conductive carbon black, and polytetrafluoroethylene (60% by weight emulsion, Aladdin) at a weight ratio of 3:1:3, and the catalyst slurry was obtained after sonication of the resultant mixture for 30 min. All measurements were carried out using a CHI760E electrochemical workstation under ambient atmosphere.

3. Theoretical calculation

Theoretical calculation was performed within the framework of density functional theory (DFT). Perdew–Burke–Ernzerhof generalized gradient approximation and the projected augmented wave method were used, which were implemented in the Vienna Ab initio Software Package (VASP 5.3.5) [27,28]. The cutoff energy for the plane-wave basis set was 400 eV. The Brillouin zone of the surface unit cell was sampled using the Monkhorst–Pack (MP) grids with a k-point mesh for Fe-N$_4$ and Fe-N$_4$ @SiO$_2$ structure optimization [29]. The Fe-N$_4$ and Fe-N$_4$ @SiO$_2$ surfaces were investigated using a 3 × 3 × 1 MP grid. The convergence criterion for the electronic self-consistent iteration and force was set to 10^{-5} eV and 0.01 eV Å^{-1}, respectively. The climbing image nudged elastic band method was used to confirm the transition states with only one imaginary frequency along the reaction coordinates [30,31].

4. Results and discussions

4.1. Material synthesis and characterization

Only the atomic catalytic sites located at the triple-phase boundary of the electrocatalyst-electrolyte-oxygen interface are effective for ORR [32]. With this in mind, we prepared a catalyst with isolated Fe atoms anchored on the surface of the CNS. This was achieved via the diffusion of Fe species through a silica shell, during which the Fe diffusion temperature and duration were carefully optimized. As shown in Fig. 1a, PDAS was first synthesized by the polymerization of dopamine monomers (SEM and TEM images for PDAS are shown in Fig. S2), which was then coated with an amorphous silica layer with a thickness of ~5 nm by the hydrolysis of tetraethyl orthosilicate (TEM image shown in Fig. S3). The resultant PDAS@SiO$_2$ was mixed with FeCl$_3$ uniformly by first soaking in solution. The two components were then ground together after water evaporation, during which FeCl$_3$ diffused through the silica shell to coordinate with amino groups in PDAS, owing to the high affinity between Fe ions and amino groups [33]. The diffusion of Fe is even more pronounced at temperatures above 306 °C. At these temperatures, FeCl$_3$ melts and migrates across the silica shell through atomic exchange. After carbonization, the product was mildly leached with HCl to remove the physically adsorbed Fe particles and subsequently leached with KOH to remove the silica layer. This material was denoted as OAC, featuring the key process in which the adsorption of Fe occurs outside the silica shell. For comparison, two other types of precursors were also used for carbonization: (1) FeCl$_3$ was first adsorbed onto PDAS and then coated with silica; (2) FeCl$_3$ was adsorbed onto PDAS and directly used as the precursor without silica coating. These products were denoted as IAC (standing for adsorption of FeCl$_3$ inside the silica layer) and UCC (standing for un-confined carbonization), respectively.

All pyrolytic products displayed a spherical morphology with an average diameter of 400 nm, which perfectly inherited the original morphology and size of the precursors (SEM images are shown in Figs. S4–S5). TEM observations revealed the presence of Fe-based nanoparticles in UCC and IAC (TEM images shown in Fig. S6), which were identified as Fe$_3$C and Fe$_3$O$_4$ through XRD, as discussed later. Intriguingly, Fe$_3$O$_4$ particles were found in IAC even after silica-confined pyrolysis. It was assumed that such aggregation is inevitable when a high content of FeCl$_3$ penetrates into the interior of the precursor. Moreover, removing all the Fe-based particles by HCl leaching is difficult, as they can be encapsulated by dense graphitic domains. In
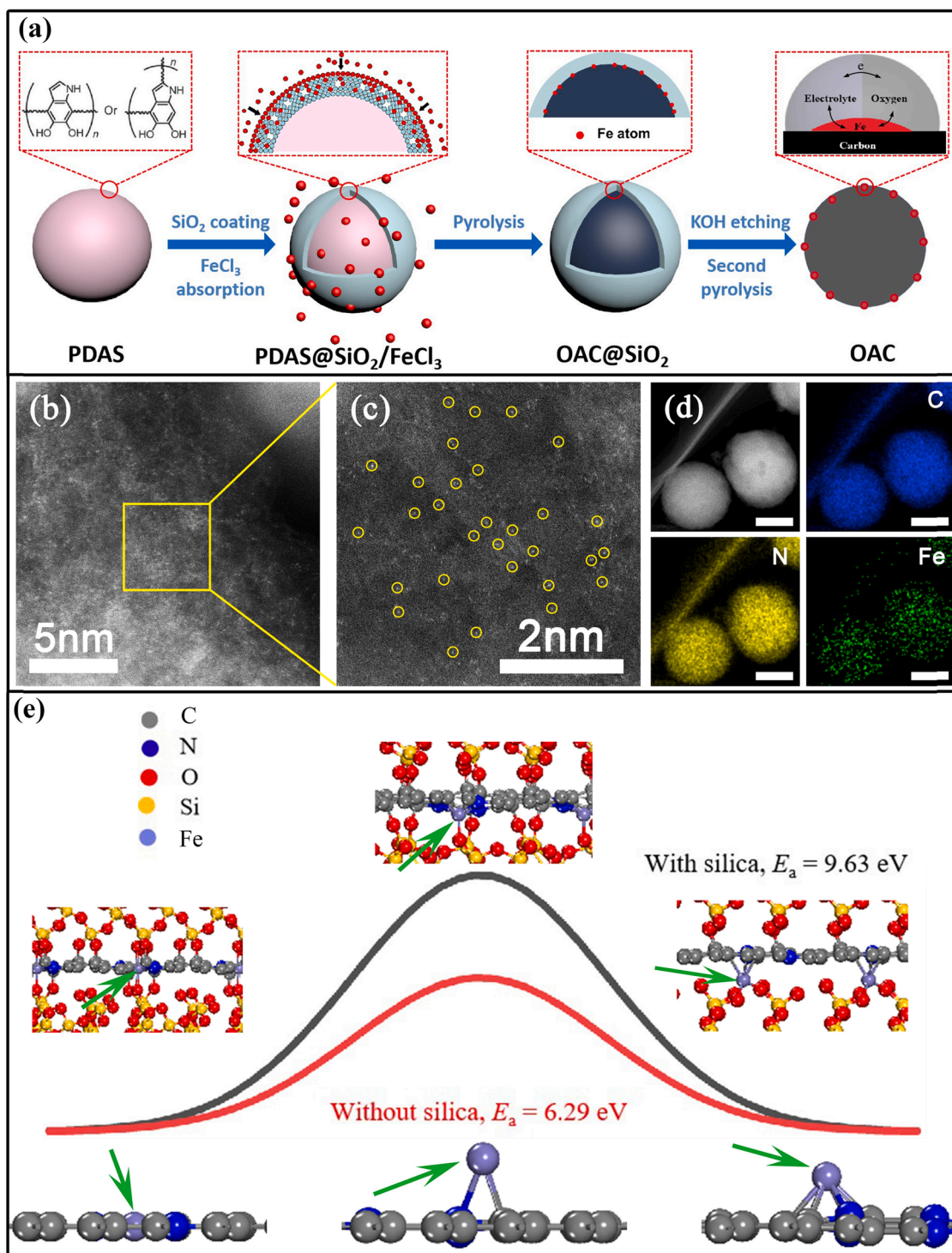
Fig. 1. (a) Schematic illustration of the preparation of CNS with single Fe atoms at the triple-phase boundary; (b) and (c) High-resolution HAADF-STEM images of the OAC; (d) Elemental mappings of OAC; (e) Migration energies of Fe atoms with and without silica confinement. The green arrows point toward Fe atoms.

contrast, no obvious nanoparticles or clusters were observed in OAC; isolated Fe single atoms were clearly identified from the aberration-corrected high-angle annular dark-field STEM (HAADF-STEM) images for this material (Fig. 1b and the bright white dots in Fig. 1c). Furthermore, elemental mapping analysis indicated that C, N, and Fe were uniformly dispersed in the CNS (Fig. 1d). During the high-temperature preparation of OAC, the Fe atoms penetrate through the amorphous silica shell by atomic exchange (FeCl$_3$ was converted into Fe(OH)$_3$ and finally into Fe$_2$O$_3$ at high temperatures, as shown in Fig. S7). This

conversion is driven by the chemical potential and/or through simple capillary adsorption into microvoids in the amorphous silica driven by the surface energy. Both processes can restrict the aggregation of Fe species at the atomic level, and thus, single atoms without any Fe particles are formed in the pyrolytic product. The effect of the chemical environment on the mobility of the Fe atoms was investigated through theoretical calculations. The calculation results suggest that the migration energy barrier (E_a) of Fe atoms in silica-confined Fe-N$_4$ (9.63 eV) is significantly higher than that in the un-confined system (6.29 eV) (side

views are shown in Fig. 1e and S8). This observation implies that the aggregation of Fe is more difficult when restricted by silica. Recently, a similar tendency was observed in silica-impregnated metal-organic framework (MOF) that contain Fe species [26]. More importantly, after diffusing through the silica shell, the Fe species only reached the outermost surface of the underlying CNS after optimizing the carbonization temperature and duration. These surface-mounted Fe single atoms can be fully accessed by the dissolved O_2 in the electrolyte, which is crucial for catalytic ORR. We also prepared Pt-OAC and Co-OAC using the same approach, replacing $FeCl_3$ with $HPtCl_6$ and $CoCl_2$, respectively. HAADF-STEM analysis confirmed the isolated atomic dispersion of Pt and Co in these samples (Fig. S9). Particularly, Fig. S9c and S9d clearly show the confinement of Co atoms on the outermost surfaces of the CNS. Thus, this strategy can be extended to a range of metallic elements and to other carbon substrates such as carbon fibers and carbon nanosheets, yielding a universal approach for the preparation of SACs with metal atoms anchored on carbon surfaces.

The XRD pattern of the OAC shows a sharp peak at 26.6°, which is attributed to the diffraction of the (002) plane of the graphitic crystallites (Fig. 2a). No other diffraction peaks related to metallic Fe or other Fe compounds were observed in this diffraction pattern. The degree of graphitization is even higher in UCC and IAC, as evidenced by the stronger and narrower diffraction peak at 26.4°. Additional diffraction

peaks were observed for these two samples, which were ascribed to Fe_3C (JSPDS Card# 35-0772), Fe_3O_4 (JSPDS Card# 19-0629) and Fe phases (JSPDS Card# 06-0696). These observations are in good agreement with the TEM results. The high graphitization degree of these samples is also corroborated by Raman spectroscopy. In addition to the D-band at 1350 cm^{-1} and G-band at 1577 cm^{-1}, which are characteristic bands of the sp^2-hybridized graphitic carbon, a well-defined 2D-band was observed in all three samples at ~2640 cm^{-1} (Fig. S10). This band is only appreciably observed in highly graphitized structures [34]. Achieving a high degree of graphitization at a low carbonization temperature is crucial for retaining the desired porous structure [35]. This porous nature was revealed by the N_2 adsorption-desorption isotherms and the corresponding pore size distribution curves (Fig. S11). The specific surface areas of OAC, IAC, and UCC were determined to be 260.1 $m^2 g^{-1}$, 444.9 $m^2 g^{-1}$, and 265.9 $m^2 g^{-1}$, respectively. Among the three materials, OAC exhibits the lowest surface area due to the lowest loading of $FeCl_3$; however, it also possesses the largest average pore size (3.5 nm), which is most favorable for the collision of oxygen with the pores and thus desired for efficient ORR [36].

The chemical compositions and valence states of the catalysts were investigated using XPS. The survey spectrum for OAC revealed the atomic contents of 89.62%, 6.32%, 3.76%, and 0.3% for C, O, N, and Fe elements, respectively (Fig. S12 and Table S1), corresponding to a
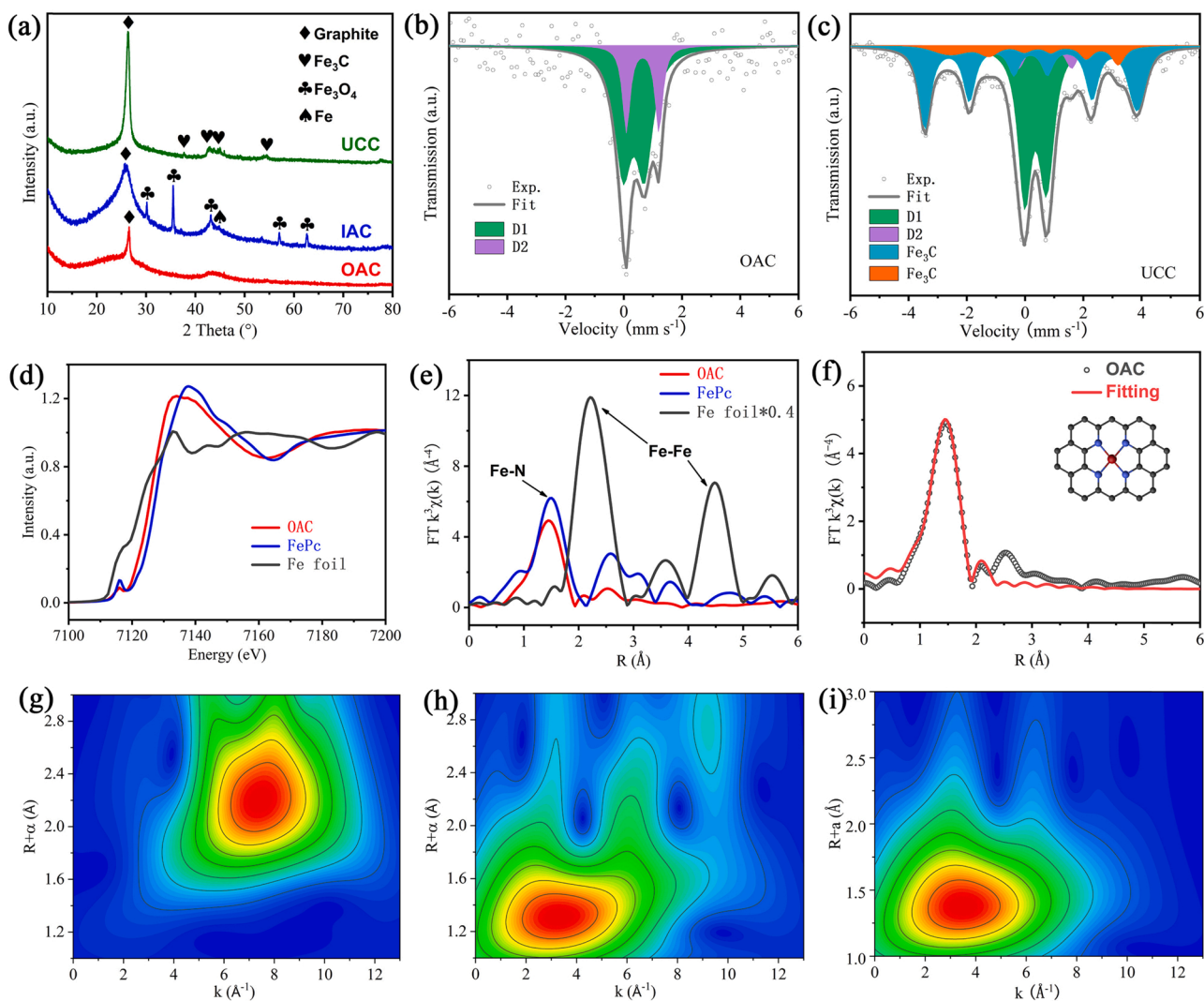

Fig. 2. Structural characterization: (a) XRD patterns; (b) and (c) ^{57}Fe Mössbauer spectra; (d) Fe K-edge XANES spectra; (e) FT curves derived from EXAFS spectra; (f) EXAFS fitting for OAC (inset: model of Fe-N$_4$. Fe, N, and C are represented by red, blue, and black spheres, respectively); WT contour plots for: (g) Fe foil, (h) FePc, and (i) OAC.

weight content of approximately 1.34% for Fe. Most importantly, when measured using ICP, the weight content of Fe was only 0.3%. This discrepancy in weight contents can be explained by the fact that the XPS technique probes a depth of only a few nanometers on the surface, whereas ICP determines the composition across the whole sample. This further suggests that the Fe single atoms are mostly mounted on the outermost surface, and those in the interior of the CNS are negligible. In comparison, the Fe contents measured by XPS for IAC and UCC were 0.34 at% and 0.38 at%, respectively. The respective values measured by ICP were 2.8 wt% and 1.5 wt%, which agree well with the XPS results, indicating that Fe is distributed more uniformly along the radial direction in these two materials.

The high-resolution N 1 s spectrum was deconvoluted into five peaks located at 398.4, 399.2, 400.2, 401.1, and 402.5 eV (Fig. S13a); these peaks were attributed to the pyridinic N, Fe-N, pyrrolic N, graphitic N, and oxidized N, respectively [37–39]. OAC possessed the highest fraction of Fe-N among the three samples (Table S2), and thus the strongest tendency to form Fe-N$_x$ sites [40,41]. This tendency was corroborated by the high-resolution Fe 2p spectrum (Fig. S13b), in which a prominent peak at 711.0 eV corresponding to Fe-N$_x$ species was observed [42]. No other peaks for metallic Fe, iron carbide, or iron oxide were detected in the OAC spectrum. In contrast, a pair of weak doublets corresponding to Fe 2p$_{3/2}$ and Fe 2p$_{1/2}$ can be observed in the Fe 2p spectrum of IAC and UCC (Fig. S14), suggesting the presence of Fe$_3$C and Fe$_x$O$_y$ species [43]. The high-resolution C 1 s spectra for all three samples show prominent peaks at 284.8 eV, attributed to sp^2-hybridized C (Fig. S15 and Table S3). These peaks suggest that a high degree of graphitization was achieved for these materials.

Mössbauer spectroscopy was employed to identify the spin states of the Fe species in these catalysts (Fig. 2b and c; the fitting parameters are listed in Table S4). The Mössbauer spectrum of OAC was deconvolved into two doublets (D1 and D2), which were assigned to the Fe-N$_4$ species and Fe atoms in high- and medium/low-spin states, respectively, suggesting the atomic dispersion of Fe without particles or metallic Fe [44–47]. Moreover, the two Fe types (D1 and D2) accounted for 75% and 25% of the total Fe species, respectively. In contrast, UCC exhibited a much higher fraction of two sextet peaks corresponding to Fe$_3$C, indicating the existence of a large amount of Fe$_3$C in UCC [44,48].

EXAFS measurements were performed to analyze the local electronic structure of OAC. The Fe K-edge XANES spectrum of OAC (Fig. 2d) exhibits a higher energy absorption region than that of Fe foil and is close to that of iron phthalocyanine (FePc), implying the existence of positively charged isolated Fe atoms. The Fourier transform (FT) curve derived from the EXAFS spectrum displays a peak at approximately ~1.5 Å, which matches the peak of FePc (Fig. 2e). Furthermore, no appreciable peak at ~2.2 Å for the Fe-Fe bond was detected. These results demonstrate the successful construction of N-coordinated Fe atomic sites in the OAC. The least-squared EXAFS fitting curves (Fig. 2f and Fig. S16) and fitting parameters (Table S5) suggest that the first shell peak at 1.5 Å corresponds to single Fe atoms with four coordinated N atoms. The inset in Fig. 2f shows a schematic diagram of the Fe-N$_4$ structure. For comparison, the fitting results for the Fe foil and FePc are shown in Fig. S17. Furthermore, wavelet transform (WT) of the Fe K-edge EXAFS oscillations was performed (Fig. 2g-i). As shown in the WT contour plots, OAC exhibits only one intensity maximum at ~ 4 Å^{-1}, which is dominated by Fe-N bonding. This observation also suggests the atomic dispersion of Fe atoms in this catalyst. The fraction of Fe-N$_4$ sites among the total Fe species (Fe-N$_4$ and Fe-containing particles) in OAC was further quantified by the linear combination fitting of the XANES spectra using pure FePc and Fe foil as references (Fig. S18) [49]. This fraction was found to be 94.2%, which implies that almost all the Fe species are in the form of single atoms. Therefore, the Mössbauer spectroscopic and EXAFS investigations confirm the facile and effective construction of atomic Fe-N$_4$ sites using the silica shell restricted diffusion method.

4.2. Electrocatalytic performance

The ORR catalytic activity of these materials is evident from the well-defined cathodic peak observed at the peak potential of 0.86 V (vs. RHE) in the CV curves acquired from O$_2$-saturated KOH solution. This peak is absent in the CV curves obtained from the N$_2$-saturated electrolytes (Fig. S19). The LSV curves suggest that OAC exhibits a more positive onset potential (E_{onset}= 0.98 V) and a higher diffusion limited current density (J_d= 6.0 mA cm^{-2}) than those of Pt/C (0.96 V and 5.5 mA cm^{-2}, respectively) and the control samples (Fig. 3a). The half-wave potential exhibited the same trend, that is, OAC ($E_{1/2}$ = 0.854 V) > Pt/C ($E_{1/2}$ = 0.824 V) > IAC ($E_{1/2}$ = 0.811 V). OAC also exhibits a lower Tafel slope (58 mV dec^{-1}) than that of the Pt/C catalyst (70 mV dec^{-1}) and IAC (91 mV dec^{-1}) in the low overpotential region (Fig. 3b), further confirming that the ORR activity of OAC is higher than that of the other catalysts. The superior performance of OAC is also reflected by its high electrochemical active surface area determined from the double layer capacitance (C_{dl}), which is in turn derived from the CV curves in the potential range of 1.2–1.3 V, where no obvious ORR occurs (Fig. S20). Moreover, the Pt-OAC and Co-OAC prepared using the same restricted diffusion approach showed excellent catalytic performances (Fig. S21), which are higher than those of the Co-particle-based catalysts reported in the literature [50].

The ORR kinetics for all materials was investigated by recording the LSV curves at different rotating speeds (Fig. S22). The electron transfer number (n) was calculated using the Koutecky-Levich (K-L) equation. OAC exhibited an n value of ~4.0 in the potential range of 0.2–0.6 V. This suggests that OAC follows an ideal 4e$^-$ ORR pathway similar to that of the benchmark Pt/C catalyst (Fig. S23). The ORR pathway was further analyzed using the RRDE. As shown in Fig. 3c, in the potential range of 0.2–0.7 V, OAC exhibits n values in the range of 3.84–3.98. These values are in excellent agreement with the result derived from the K-L plots, confirming that the catalytic process of the OAC follows a 4e$^-$ ORR pathway. The corresponding H$_2$O$_2$ yields were found to be 0.90–8.14%, which are comparable to those of Pt/C (2.06–8.07%).

The long-term stability of the catalysts was evaluated by repeated CV scans in the potential range of 0.4–1.0 V at a scan rate of 0.1 V s^{-1} for 30,000 cycles. The LSV curves recorded before and after the long-term operation are shown in Fig. 3d. The onset potential of OAC was shifted negatively by 72 mV, indicating an obvious decay of the performance after 30,000 cycles' operation. However, the diffusion-limited current only decreased slightly, which suggests the durability of the catalyst is relatively satisfying compared to the other SACs reported previously. After the long-term operation, the microstructure of the catalyst was again inspected using TEM. As shown in Fig. S24, the atomic Fe is still bound in the carbon matrix after 30,000 cycles (100 h of operation). This structure is similar to that of the fresh catalyst before the durability test. In addition, no Fe was detected using ICP from the electrolyte solution, again confirming that the Fe atomic sites were firmly anchored on the carbon matrix and did not dissolve into the solution. The OAC also showed good tolerance to methanol interruption. After injecting 1 M methanol into the electrolyte, OAC maintained a relatively stable current density, whereas Pt/C showed an abrupt decrease in the current (Fig. S25). These results indicate that OAC is superior to the benchmark Pt/C catalyst in terms of fuel selectivity.

Furthermore, OAC also demonstrated outstanding ORR performance in acidic electrolytes, which is critical for practical applications. Here, OAC exhibited an E_{onset} of 0.86 V, an $E_{1/2}$ of 0.71 V, a J_k of 6.57 mA cm^{-2}, a Tafel slope of 61 mV dec^{-1}, an n value of 3.95, H$_2$O$_2$ yields lower than 5.6%, almost unperturbed current upon methanol injection, and a current decrease of 12% after 20,000 s' operation in 0.1 M HClO$_4$ (Figs. S26–S28). These metrics, while outperforming those of the control samples, are comparable or even superior to the leading results reported in the literature for carbon-supported non-precious metal catalysts and another important type of electrocatalyst based on non-van der Waals 2D materials [51–54]. To name a few, an Fe-SAC
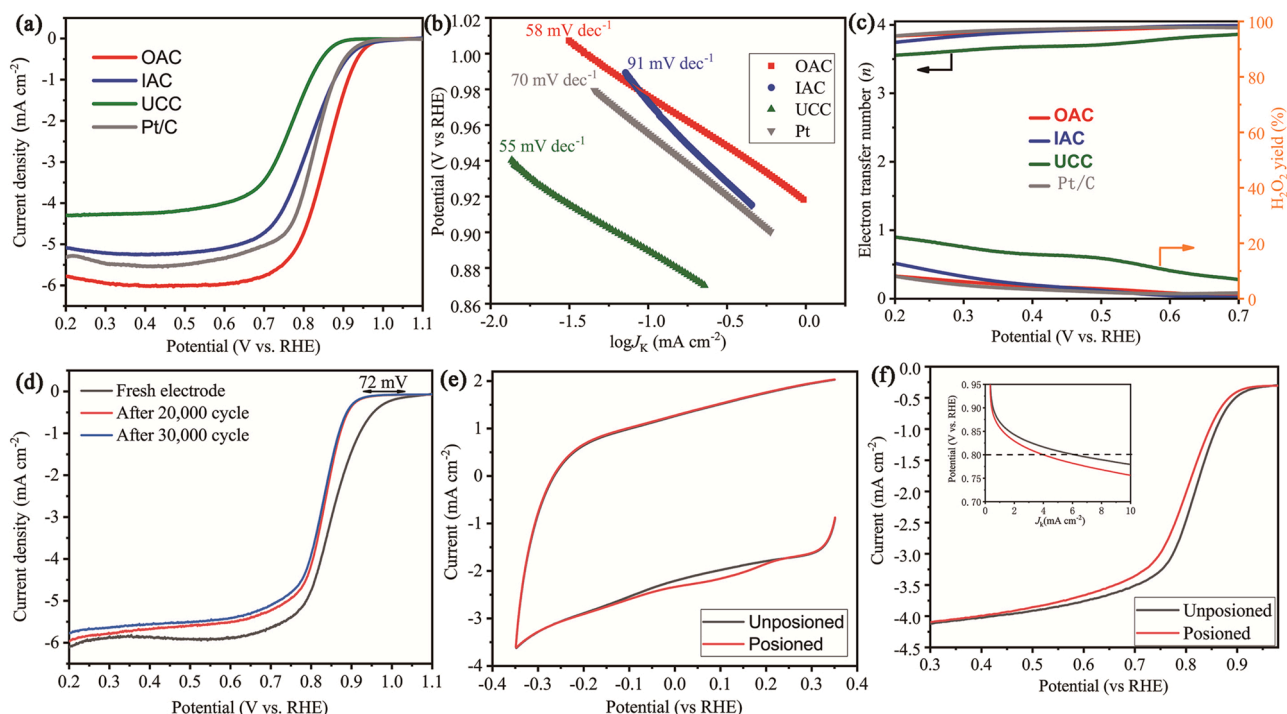
Fig. 3. (a) LSV curves acquired in O_2-saturated 0.1 M KOH; (b) Tafel plots; (c) H_2O_2 yields and electron transfer number measured by RRDE; (d) Long-term stability measurements; (e) CV curves of OAC before and after nitrite adsorption in the nitrite reductive stripping region in a N_2-saturated 0.5 M acetate buffer at pH 5.2; (f) LSV curves of OAC before and after nitrite adsorption in an O_2-saturated 0.5 M acetate buffer at pH 5.2. Rotating speed: 1600 rpm; Sweep rate: 10 mV s^{-1}; Mass loadings in (a–d): 0.32 mg cm^{-2} and in (e–f): 0.27 mg cm^{-2}.

derived from the macrocycle cucurbit[6]uril showed an E_{onset} of 0.94 V and a J_d of 5.6 mA cm^{-2} [53], and a catalyst based on iron phthalocyanine/defective graphene exhibited an E_{onset} of 0.98 V and a J_d of 5.45 mA cm^{-2} in alkaline media [55] (Tables S6 and S7).

To identify the active sites in OAC, SCN$^-$, which has a strong affinity for Fe ions but has less impact on Fe particles or Fe-free sites [40,56], was employed to analyze the catalytic process. The $E_{1/2}$ of OAC was negatively shifted by 31 mV and 120 mV after poisoning by 10 mM KSCN in KOH and HClO$_4$, respectively (Fig. S29), accompanied by a decrease in the kinetic current density in both media. These results confirm that single atomic Fe sites (namely Fe-N$_4$) are responsible for the excellent ORR activity of OAC. More importantly, the active site density was further quantified using nitrite stripping test established by Malko et al. [18,57], which is based on the fact that nitrite anions can bind strongly with accessible Fe-N$_4$ sites to form stable poisoned adducts. However, the poisons can be stripped off at a low potential to recover the catalytic activity. Hence, the use of nitrite anions leads to a strong and reversible poisoning. This in-situ electrochemical method generally yields a much lower value for the site density than the gaseous probes (such as CO and NO), but is more convenient and might better represent the actual reactions occurring on the catalyst [19]. As shown in Fig. 3e, the CV curves for OAC in a 0.5 M acetate buffer before and after adsorption of nitrite overlap; however, the latter exhibits a broad peak corresponding to nitrite reduction in the potential range of − 0.3–0.2 V. The excess coulometric charge due to nitrite reduction was then used to quantify the SD, which was found to be 42.9 μmol g^{-1}. Fig. 3f shows the corresponding kinetic currents, from which the TOF was determined to be 1.87 s^{-1} at 0.8 V, which is a typical value for the intrinsic activity of atomic Fe-N$_4$ sites [19]. While the gravimetric SD here is only moderate compared to the literature data [17], it corresponds to a remarkable 80% UE of the Fe sites in our OAC catalyst, which is among the highest compared with the recently reported results [17–21]. For example, a recent cross-laboratory investigation into four typical Fe-SACs suggested that the effective Fe atoms in these catalysts are all below 10% because

conventional pyrolysis-and-leach methods bury most of the sites in the carbon matrix [19]. A very recent study by Jiao et al. demonstrated an Fe-SAC with a UE of 100%, which was prepared by substituting Zn atoms with Fe in a ZIF-derived catalyst through a gas phase trans-metalation method, suggesting that atomic sites are only effective in an open structure [22]. More importantly, considering that the nitrite reduction method generally underestimates the active site density by a factor of ∼30% due to that there are multiple types of Fe-N$_x$ sites and nitrite only probes a fraction of them [19], a UE of 80% for the OAC suggests that approximately all the Fe atomic sites are fully exposed. The coincidence between the UE quantified herein and the fraction of high-spin D1 type Fe sites among the total Fe content determined by Mössbauer spectroscopy (75%) suggests that nitrite might be most sensitive to D1 type Fe, which in turn indicates that it is the high-spin Fe that contributes predominantly to the ORR activity. The high UE of OAC is associated with the distribution of Fe atomic sites on the outermost surface, which is enabled by restricted diffusion through the silica shell during the pyrolysis process. Overall, this extraordinary UE endows a good catalytic performance at an extremely low metallic center content.

Encouraged by the excellent catalytic performance, we assembled primary Zn-air batteries using OAC (loaded on nickel foam) as the air cathode (Fig. 4a). The OAC battery exhibited an open-circuit potential (OCP) of 1.49 V, which is higher than that of Pt/C- (1.46 V), IAC- (1.44 V), and UCC- (1.43 V) based primary Zn-air batteries (Fig. S30). Fig. 4b presents the polarization curves and the corresponding power densities for the Zn-air batteries. The OAC battery exhibits a peak power density of 113 mW cm^{-2}, which is typical of a device based on state-of-the-art non-precious metal catalysts [58–61], and higher than those based on Pt/C (100 mW cm^{-2}), IAC (103 mW cm^{-2}), and UCC (59 mW cm^{-2}). Galvanostatic discharge measurements reveal that the OAC battery displays potential platforms at 1.35, 1.30, 1.25, and 1.16 V at discharge current densities of 2, 5, 10, and 20 mA cm^{-2} (Fig. 4c), respectively. Furthermore, the OAC battery exhibited a specific capacity of 710 mAh g$_{Zn}^{-1}$ at 5 mA cm^{-2} and 691 mAh g$_{Zn}^{-1}$ at 25 mA cm^{-2}
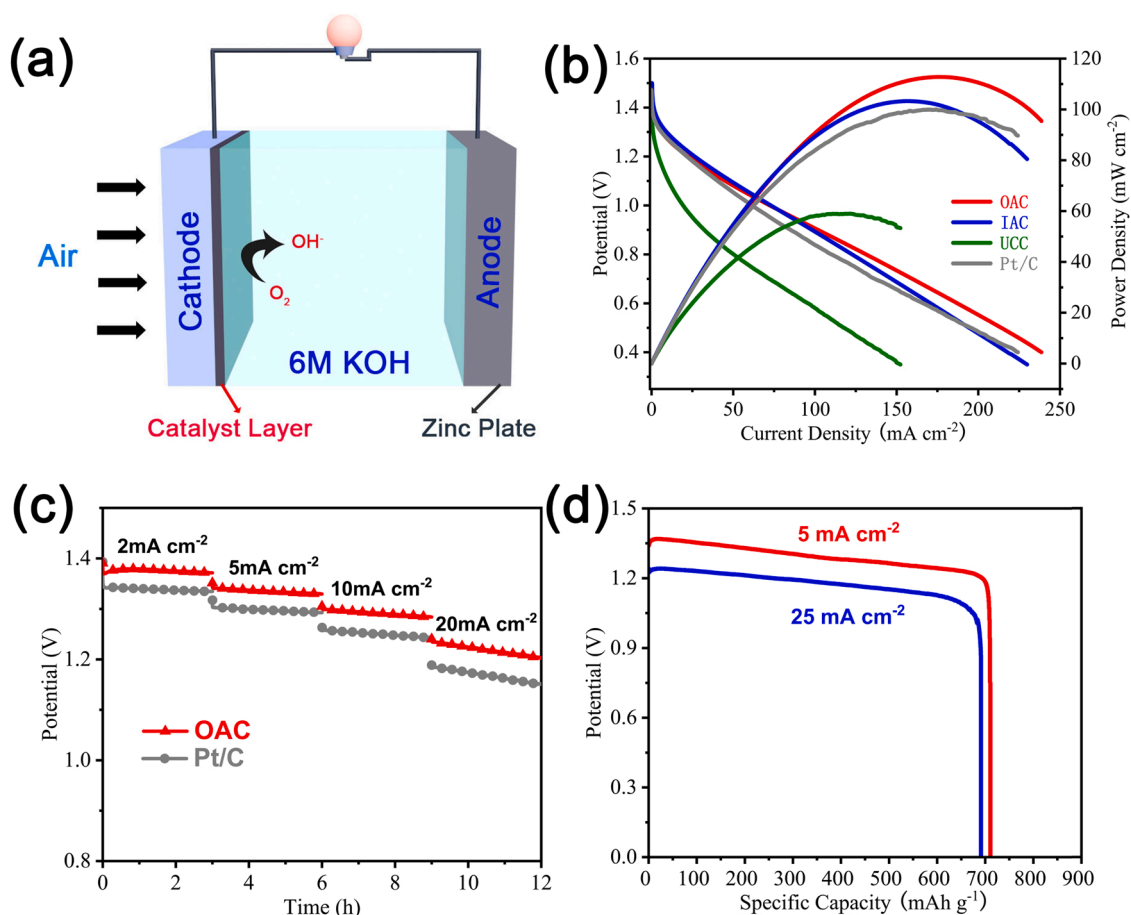
Fig. 4. (a) Schematic configuration of the Zn-air battery; (b) Polarization curves and corresponding power density curves of the batteries constructed with different catalysts; (c) Galvanostatic discharge curves of the batteries at different current densities; (d) Specific capacities of the OAC-based battery at current densities of 5 and 25 mA cm^{-2}.

(Fig. 4d), thus demonstrating its excellent performance at high current densities. Two OAC batteries connected in series can light up a blue light-emitting diode (Fig. S31), demonstrating their promising potential for use in primary Zn-air batteries.

Finally, we analyzed the economic utilization of the metal source in our restricted diffusion preparation strategy. Approximately 0.8% of the starting Fe was successfully incorporated into the final OAC material. The major loss of the Fe source, occurred during the mild HCl leaching of the pyrolytic composites, can be easily separated and from the silica-coated CNS by vacuum filtration. The FeCl$_3$ solution was then used directly as the Fe source to prepare the SACs again. This recycling process is environmentally benign and cost effective, in which the only chemical used, HCl, can be easily recycled through evaporation-and-absorption in industrial production. Regarding the valuable metal source, ~87% of the starting Fe can be recovered in this facile protocol. The lost Fe species could be due to evaporation during the stabilization stage (at 400 °C), the diffusion of FeCl$_3$ into the crucible and those encapsulated in the silica shell. We believe even more Fe can be recovered in the future by optimizing the pyrolysis process (e.g. stabilizing at 300 °C) and by using a Cu-coated ceramic crucible (those in the silica shell, accounting for ~1.4% of the total Fe, might not be worth to recover due to possible environmental pollution and high costs). Most importantly, the OAC prepared from the recycled Fe compounds exhibited similar morphology, composition, and catalytic performance as those prepared using fresh FeCl$_3$ (Figs. S32–S33). These results suggest that our preparation method is compatible with various grades of metal sources, and thus it is a metal-saving approach.

5. Conclusion

In summary, CNS-based catalysts with single atomic metals (Fe, Pt, and Co) dispersed on the surface were prepared by combining restricted diffusion and confined pyrolysis. Single atoms without any particles were formed because the silica shell restricts the aggregation of metallic species at the atomic level. Anchoring on the surface endowed an exceptionally high accessibility of the atomic sites, which in turn enabled the outstanding catalytic performance of Fe-SACs towards ORR, with an onset potential of 0.98 V and an ideal 4e$^-$ pathway. This was accomplished using an extremely low loading of metallic species. In addition, the porous structure and high degree of graphitization of the carbon support enabled a power density of 113 mW cm^{-2} and a specific capacity of 710 mAh g$_{Zn}^{-1}$ for the constructed Zn-air battery. We demonstrated that this strategy can be extended to prepare other carbon-based electrocatalysts with various single-atom metallic active sites exposed on the surface. Moreover, this versatile strategy can potentially accommodate various carbon substrates, such as one-dimensional carbon fibers and two-dimensional nanosheets. This approach could remarkably reduce the amount of metals required for high catalytic efficiency and thus the cost of the catalysts, which would ultimately boost their practical applications for a range of electro-catalytic processes, such as fuel cells, metal-air batteries, CO$_2$ reduction reaction, electro-synthesis and so on.

CRediT authorship contribution statement

Libo Deng: Conceptualization, Writing – original draft. **Lei Qiu**:

Investigation, Writing. **Rong Hu**: Methodology. **Lei Yao**: Conceptualization, Supervision. **Zijian Zheng**: Writing – review & editing. **Xiangzhong Ren**: Writing – review & editing. **Yongliang Li**: Validation. **Chuanxin He**: Data analysis, Supervision.

Declaration of Competing Interest

The authors declare no competing interests.

Appendix A. Supporting information

Supplementary data associated with this article can be found in the online version at doi:10.1016/j.apcatb.2021.121058.

References

[1] S. Ji, Y. Chen, X. Wang, Z. Zhang, D. Wang, Y. Li, Chemical synthesis of single atomic site catalysts, Chem. Rev. 120 (2020) 11900–11955, https://doi.org/10.1021/acs.chemrev.9b00818.

[2] A. Wang, J. Li, T. Zhang, Heterogeneous single-atom catalysis, Nat. Rev. Chem. 2 (2020) 65–81, https://doi.org/10.1038/s41570-018-0010-1.

[3] D.T. Tran, D.C. Nguyen, H.T. Le, T. Kshetri, V.H. Hoa, T.L.L. Doan, N.H. Kim, J.H. Lee, Recent progress on single atom/sub-nano electrocatalysts for energy applications, Prog. Mater. Sci. 115 (2021), 100711, https://doi.org/10.1016/j.pmatsci.2020.100711.

[4] V. Jose, H. Hu, E. Edison, W. Manalastas, H. Ren, P. Kidkhunthod, S. Sreejith, A. Jayakumar, J.M.V. Nsanzimana, M. Srinivasan, J. Choi, J.-M. Lee, Modulation of single atomic Co and Fe sites on hollow carbon nanospheres as oxygen electrodes for rechargeable Zn–Air batteries, Small Methods 5 (2021), 2000751, https://doi.org/10.1002/smtd.202000751.

[5] A.I. Douka, H. Yang, L. Huang, S. Zaman, T. Yue, W. Guo, B. You, B.Y. Xia, Transition metal/carbon hybrids for oxygen electrocatalysisin rechargeable zinc-air batteries, EcoMat 3 (2021), e12067, https://doi.org/10.1002/eom2.12067.

[6] E. Luo, H. Zhang, X. Wang, L. Gao, L. Gong, T. Zhao, Z. Jin, J. Ge, Z. Jiang, C. Liu, W. Xing, Single-atom Cr−N4 sites designed for durable oxygen reduction catalysis in acid media, Angew. Chem. Int. Ed. 58 (2019) 12469–12475, https://doi.org/10.1002/anie.201906289.

[7] S. Jin, Y. Ni, Z. Hao, K. Zhang, Y. Lu, Z. Yan, Y. Wei, Y.-R. Lu, T.-S. Chan, J. Chen, A universal graphene quantum dot-tethering design strategy to synthesize single-atom catalysts, Angew. Chem. Int. Ed. 59 (2020) 21885–21889, https://doi.org/10.1002/anie.202008422.

[8] D. Liu, X. Li, S. Chen, H. Yan, C. Wang, C. Wu, Y.A. Haleem, S. Duan, J. Lu, B. Ge, P.M. Ajayan, Y. Luo, J. Jiang, L. Song, Atomically dispersed platinum supported on curved carbon supports for efficient electrocatalytic hydrogen evolution, Nat. Energy 4 (2019) 512–518, https://doi.org/10.1038/s41560-019-0402-6.

[9] Y. Cheng, S. He, S. Lu, J.-P. Veder, B. Johannessen, L. Thomsen, M. Saunders, T. Becker, R.D. Marco, Q. Li, S.-Z. Yang, S.P. Jiang, Iron single atoms on graphene as nonprecious metal catalysts for high-temperature polymer electrolyte membrane fuel cells, Adv. Sci. 6 (2019), 1802066, https://doi.org/10.1002/advs.201802066.

[10] L. Zhao, Y. Zhang, L.-B. Huang, X.-Z. Liu, Q.-H. Zhang, C. He, Z.-Y. Wu, L.-J. Zhang, J. Wu, W. Yang, L. Gu, J.-S. Hu, L.-J. Wan, Cascade anchoring strategy for general mass production of high-loading single-atomic metal-nitrogen catalysts, Nat. Commun. 10 (2019) 1278, https://doi.org/10.1038/s41467-019-09290-y.

[11] Y.Z. Zhou, X.F. Tao, G.B. Chen, R.H. Lu, D. Wang, M.X. Chen, E.Q. Jin, J. Yang, H.W. Liang, Y. Zhao, X.L. Feng, A. Narita, K. Mullen, Multilayer stabilization for fabricating high-loading single-atom catalysts, Nat. Commun. 11 (2020) 5892, https://doi.org/10.1038/s41467-020-19599-8.

[12] Q. Wang, Y. Yang, F. Sun, G. Chen, J. Wang, L. Peng, W.-T. Chen, L. Shang, J. Zhao, D. Sun-Waterhouse, T. Zhang, G.I.N. Waterhouse, Molten NaCl-assisted synthesis of porous Fe-N-C electrocatalysts with a high density of catalytically accessible FeN4 active sites and outstanding oxygen reduction reaction performance, Adv. Energy Mater. 11 (2021), 2100219, https://doi.org/10.1002/aenm.202100219.

[13] J.N. Guo, B.J. Li, Q.Y. Zhang, Q.T. Liu, Z.L. Wang, Y.F. Zhao, J.L. Shui, Z.H. Xiang, Highly accessible atomically dispersed Fe-N-x sites electrocatalyst for proton-exchange membrane fuel cell, Adv. Sci. 8 (2021), 2002249, https://doi.org/10.1002/advs.202002249.

[14] X. Fu, P. Zamani, J.-Y. Choi, F.M. Hassan, G. Jiang, D.C. Higgins, Y. Zhang, M.A. Hoque, Z. Chen, In situ polymer graphenization ingrained with nanoporosity in a nitrogenated electrocatalyst boosting the performance of polymer-electrolyte-membrane fuel cells, Adv. Mater. 29 (2017), 1604456, https://doi.org/10.1002/adma.201604456.

[15] J. Han, H. Bao, J.-Q. Wang, L. Zheng, S. Sun, Z.L. Wang, C. Sun, 3D N-doped ordered mesoporous carbon supported single-atom Fe-N-C catalysts with superior performance for oxygen reduction reaction and zinc-air battery, Appl. Catal. B Environ. 280 (2021), 119411, https://doi.org/10.1016/j.apcatb.2020.119411.

[16] Y. Ye, F. Cai, H. Li, H. Wu, G. Wang, Y. Li, S. Miao, S. Xie, R. Si, J. Wang, X. Bao, Surface functionalization of ZIF-8 with ammonium ferric citrate toward high exposure of Fe-N active sites for efficient oxygen and carbon dioxide electroreduction, Nano Energy 38 (2017) 281–289, https://doi.org/10.1016/j.nanoen.2017.05.042.

[17] X. Wan, X. Liu, Y. Li, R. Yu, L. Zheng, W. Yan, H. Wang, M. Xu, J. Shui, Fe-N-C electrocatalyst with dense active sites and efficient mass transport for high-performance proton exchange membrane fuel cells, Nat. Catal. 2 (2018) 259–268, https://doi.org/10.1038/s41929-019-0237-3.

[18] D. Malko, A. Kucernak, T. Lopes, In situ electrochemical quantification of active sites in Fe-N/C non-precious metal catalysts, Nat. Commun. 7 (2016) 13285, https://doi.org/10.1038/ncomms13285.

[19] M. Primbs, Y. Sun, A. Roy, D. Malko, A. Mehmood, M.-T. Sougrati, P.-Y. Blanchard, G. Granozzi, T. Kosmala, G. Daniel, P. Atanassov, J. Sharman, C. Durante, A. Kucernak, D. Jones, F. Jaouen, P. Strasser, Establishing reactivity descriptors for platinum group metal (PGM)-free Fe-N-C catalysts for PEM fuel cells, Energy Environ. Sci. 13 (2020) 2480–2500, https://doi.org/10.1039/d0ee01013h.

[20] W. Xie, Y. Song, S. Li, J. Li, Y. Yang, W. Liu, M. Shao, M. Wei, Single-atomic-Co electrocatalysts with self-supported architecture toward oxygen-involved reaction, Adv. Funct. Mater. 29 (2019), 1906477, https://doi.org/10.1002/adfm.201906477.

[21] L. Chen, X. Liu, L. Zheng, Y. Li, X. Guo, X. Wan, Q. Liu, J. Shang, J. Shui, Insights into the role of active site density in the fuel cell performance of Co-N-C catalysts, Appl. Catal. B Environ. 256 (2019) 117849, https://doi.org/10.1016/j.apcatb.2019.117849.

[22] L. Jiao, J. Li, L.L. Richard, Q. Sun, T. Stracensky, E. Liu, M.T. Sougrati, Z. Zhao, F. Yang, S. Zhong, H. Xu, S. Mukerjee, Y. Huang, D.A. Cullen, J.H. Park, M. Ferrandon, D.J. Myers, F. Jaouen, Q. Jia, Chemical vapour deposition of Fe–N–C oxygen reduction catalysts with full utilization of dense Fe-N4 sites, Nat. Mater. 20 (2021) 1385–1391, https://doi.org/10.1038/s41563-021-01030-2.

[23] M. Liu, J. Liu, Y. Song, Z. Li, F. Wang, Mononuclear iron-dependent electrocatalytic activity of metal-nitrogen-carbon catalysts for efficient oxygen reduction reaction, Appl. Catal. A Gen. 583 (2019), 117120, https://doi.org/10.1016/j.apcata.2019.117120.

[24] B.-C. Hu, Z.-Y. Wu, S.-Q. Chu, H.-W. Zhu, H.-W. Liang, J. Zhang, S.-H. Yu, SiO2-protected shell mediated templating synthesis of Fe-N-doped carbon nanofibers and their enhanced oxygen reduction reaction performance, Energy Environ. Sci. 11 (2018) 2208–2215, https://doi.org/10.1039/C8EE00673C.

[25] Y.J. Sa, D.-J. Seo, J. Woo, J.T. Lim, J.Y. Cheon, S.Y. Yang, J.M. Lee, D. Kang, T.J. Shin, H.S. Shin, H.Y. Jeong, C.S. Kim, M.G. Kim, T.-Y. Kim, S.H. Joo, A general approach to preferential formation of active Fe-Nx sites in Fe-N/C electrocatalysts for efficient oxygen reduction reaction, J. Am. Chem. Soc. 138 (2016) 15046–15056, https://doi.org/10.1021/jacs.6b09470.

[26] L. Jiao, R. Zhang, G. Wan, W. Yang, X. Wan, H. Zhou, J. Shui, S.-H. Yu, H.-L. Jiang, Nanocasting SiO2 into metal-organic frameworks imparts dual protection to high-loading Fe single-atom electrocatalysts, Nat. Commun. 11 (2020) 2831, https://doi.org/10.1038/s41467-020-16715-6.

[27] J.P. Perdew, K. Burke, M. Ernzerhof, Generalized gradient approximation made simple, Phys. Rev. Lett. 77 (1996) 3865–3868, https://doi.org/10.1103/PhysRevLett.77.3865.

[28] B. Hammer, L.B. Hansen, J.K. Nørskov, Improved adsorption energetics within density-functional theory using revised Perdew-Burke-Ernzerhof functionals, Phys. Rev. B 59 (1999) 7413–7421, https://doi.org/10.1103/PhysRevB.59.7413.

[29] H.J. Monkhorst, J.D. Pack, Special points for Brillouin-zone integrations, Phys. Rev. B 13 (1976) 5188–5192, https://doi.org/10.1103/PhysRevB.13.5188.

[30] G. Henkelman, H. Jonsson, Improved tangent estimate in the nudged elastic band method for finding minimum energy paths and saddle points, J. Chem. Phys. 113 (2000) 9978–9985, https://doi.org/10.1063/1.1323224.

[31] D. Sheppard, G. Henkelman, Paths to which the Nudged Elastic Band Converges, J. Comput. Chem. 32 (2011) 1769–1771, https://doi.org/10.1002/jcc.21748.

[32] M. Qiao, M.-M. Titirici, Engineering the interface of carbon electrocatalysts at the triple point for enhanced oxygen reduction reaction, Chem. Eur. J. 24 (2018) 18374–18384, https://doi.org/10.1002/chem.201804610.

[33] C. Gao, Q. Zhang, Z. Lu, Y. Yin, Templated synthesis of metal nanorods in silica nanotubes, J. Am. Chem. Soc. 133 (2011) 19706–19709, https://doi.org/10.1021/ja209647d.

[34] A. Sadezky, H. Muckenhuber, H. Grothe, R. Niessner, U. Pöschl, Raman microspectroscopy of soot and related carbonaceous materials: spectral analysis and structural information, Carbon 43 (2005) 1731–1742, https://doi.org/10.1016/j.carbon.2005.02.018.

[35] J. Chu, Y. Wang, F. Zhong, X. Feng, W. Chen, X. Ai, H. Yang, Y. Cao, Metal/covalent-organic frameworks for electrochemical energy storage applications, EcoMat 3 (2021) 1–32, https://doi.org/10.1002/eom2.12133.

[36] Z. Mo, W. Yang, S. Gao, J.K. Shang, Y. Ding, W. Sun, Q. Li, Efficient oxygen reduction reaction by a highly porous, nitrogen-doped carbon sphere electrocatalyst through space confinement effect in nanopores, J. Adv. Ceram. 10 (2021) 40145, https://doi.org/10.1007/s40145-021-0466-1.

[37] L. Jiao, G. Wan, R. Zhang, H. Zhou, S.-H. Yu, H.-L. Jiang, From metal–organic frameworks to single-atom Fe implanted N-doped porous carbons: efficient oxygen reduction in both alkaline and acidic media, Angew. Chem. Int. Ed. 57 (2018) 8525–8529, https://doi.org/10.1002/anie.201803262.

[38] H. Yang, Y. Wu, Q. Lin, L. Fan, X. Chai, Q. Zhang, J. Liu, C. He, Z. Lin, Composition tailoring via N and S co-doping and structure tuning by constructing hierarchical pores: metal-free catalysts for high-performance electrochemical reduction of CO_2, Angew. Chem. Int. Ed. 57 (2018) 15476–15480, https://doi.org/10.1002/anie.201809255.

[39] X. Xu, Z. Xia, X. Zhang, R. Sun, X. Sun, H. Li, C. Wu, J. Wang, S. Wang, G. Sun, Atomically dispersed Fe-N-C derived from dual metal-organic frameworks as efficient oxygen reduction electrocatalysts in direct methanol fuel cells, Appl. Catal. B Environ. 259 (2019), 118042, https://doi.org/10.1016/j.apcatb.2019.118042.

[40] Y. Chen, S. Ji, Y. Wang, J. Dong, W. Chen, Z. Li, R. Shen, L. Zheng, Z. Zhuang, D. Wang, Y. Li, Isolated single iron atoms anchored on N-doped porous carbon as an efficient electrocatalyst for the oxygen reduction reaction, Angew. Chem. Int. Ed. 56 (2017) 6937–6941, https://doi.org/10.1002/anie.201702473.

[41] J. Guo, J. Huo, Y. Liu, W. Wu, Y. Wang, M. Wu, H. Liu, G. Wang, Nitrogen-doped porous carbon supported nonprecious metal single-atom electrocatalysts: from synthesis to application, Small Methods 0 (2019) 1900159, https://doi.org/10.1002/smtd.201900159.

[42] Z. Qiao, H. Zhang, S. Karakalos, S. Hwang, J. Xue, M. Chen, D. Su, G. Wu, 3D polymer hydrogel for high-performance atomic iron-rich catalysts for oxygen reduction in acidic media, Appl. Catal. B Environ. 219 (2017) 629–639, https://doi.org/10.1016/j.apcatb.2017.08.008.

[43] Z.Y. Wu, X.X. Xu, B.C. Hu, H.W. Liang, Y. Lin, L.F. Chen, S.H. Yu, Iron carbide nanoparticles encapsulated in mesoporous Fe-N-doped carbon nanofibers for efficient electrocatalysis, Angew. Chem. Int. Ed. 54 (2015) 8179–8183, https://doi.org/10.1002/anie.201502173.

[44] U.I. Kramm, M. Lefèvre, N. Larouche, D. Schmeisser, J.-P. Dodelet, Correlations between mass activity and physicochemical properties of Fe/N/C catalysts for the ORR in PEM fuel cell via 57Fe Mössbauer spectroscopy and other techniques, J. Am. Chem. Soc. 136 (2014) 978–985, https://doi.org/10.1021/ja410076f.

[45] H. Shen, E. Gracia-Espino, J. Ma, H. Tang, X. Mamat, T. Wagberg, G. Hu, S. Guo, Atomically FeN2 moieties dispersed on mesoporous carbon: a new atomic catalyst for efficient oxygen reduction catalysis, Nano Energy 35 (2017) 9–16, https://doi.org/10.1016/j.nanoen.2017.03.027.

[46] U.I. Kramm, J. Herranz, N. Larouche, T.M. Arruda, M. Lefèvre, F. Jaouen, P. Bogdanoff, S. Fiechter, I. Abs-Wurmbach, S. Mukerjee, J.-P. Dodelet, Structure of the catalytic sites in Fe/N/C-catalysts for O2-reduction in PEM fuel cells, Phys. Chem. Chem. Phys. 14 (2012) 11673–11688, https://doi.org/10.1039/C2CP41957B.

[47] W. Zhong, J. Chen, P. Zhang, L. Deng, L. Yao, X. Ren, Y. Li, H. Mi, L. Sun, Air plasma etching towards rich active sites in Fe/N-porous carbon for the oxygen reduction reaction with superior catalytic performance, J. Mater. Chem. A 5 (2017) 16605–16610, https://doi.org/10.1039/C7TA05035F.

[48] Z. Zhang, J. Sun, F. Wang, L. Dai, Efficient oxygen reduction reaction (ORR) catalysts based on single iron atoms dispersed on a hierarchically structured porous carbon framework, Angew. Chem. Int. Ed. 57 (2018) 9038–9043, https://doi.org/10.1002/anie.201804958.

[49] Y.J. Sa, D.-J. Seo, J. Woo, J.T. Lim, J.Y. Cheon, S.Y. Yang, J.M. Lee, D. Kang, T. J. Shin, H.S. Shin, H.Y. Jeong, C.S. Kim, M.G. Kim, T.-Y. Kim, S.H. Joo, A general approach to preferential formation of active Fe–Nx sites in Fe–N/C electrocatalysts for efficient oxygen reduction reaction, J. Am. Chem. Soc. 138 (2016) 15046–15056, https://doi.org/10.1021/jacs.6b09470.

[50] X. Hu, Y. Chen, M. Zhang, G. Fu, D. Sun, J.-M. Lee, Y. Tang, Alveolate porous carbon aerogels supported Co9S8 derived from a novel hybrid hydrogel for bifunctional oxygen electrocatalysis, Carbon 144 (2019) 557–566.

[51] G. Fu, J. Wang, Y. Chen, Y. Liu, Y. Tang, J.B. Goodenough, J.-M. Lee, Exploring indium-based ternary thiospinel as conceivable high-potential air-cathode for rechargeable Zn–Air batteries, Adv. Energy Mater. 8 (2018), 1802263, https://doi.org/10.1002/aenm.201802263.

[52] V. Jose, J.M.V. Nsanzimana, H. Hu, J. Choi, X. Wang, J.-M. Lee, Highly efficient oxygen reduction reaction activity of N-doped carbon–cobalt boride heterointerfaces, Adv. Energy Mater. 11 (2021), 2100157, https://doi.org/10.1002/aenm.202100157.

[53] H. Wang, J. Chen, Y. Lin, X. Wang, J. Li, Y. Li, L. Gao, L. Zhang, D. Chao, X. Xiao, J.-M. Lee, Electronic modulation of non-van der Waals 2D electrocatalysts for efficient energy conversion, Adv. Mater. 33 (2021), 2008422, https://doi.org/10.1002/adma.202008422.

[54] P. Prabhu, J.-M. Lee, Metallenes as functional materials in electrocatalysis, Chem. Soc. Rev. 50 (2021) 6700–6719, https://doi.org/10.1039/d0cs01041c.

[55] X. Yu, S. Lai, S. Xin, S. Chen, X. Zhang, X. She, T. Zhan, X. Zhao, D. Yang, Coupling of iron phthalocyanine at carbon defect site via π-π stacking for enhanced oxygen reduction reaction, Appl. Catal. B Environ. 280 (2021) 119437, https://doi.org/10.1016/j.apcatb.2020.119437.

[56] Z. Li, L. Wei, W.-J. Jiang, Z. Hu, H. Luo, W. Zhao, T. Xu, W. Wu, M. Wu, J.-S. Hu, Chemical state of surrounding iron species affects the activity of Fe-Nx for electrocatalytic oxygen reduction, Appl. Catal. B Environ. 251 (2019) 240–246, https://doi.org/10.1016/j.apcatb.2019.03.046.

[57] D. Malko, A. Kucernak, T. Lopes, Performance of Fe-N/C oxygen reduction electrocatalysts toward NO2-, NO, and NH2OH electroreduction: from fundamental insights into the active center to a new method for environmental nitrite destruction, J. Am. Chem. Soc. 138 (2016) 16056–16068.

[58] G. Fu, Y. Wang, Y. Tang, K. Zhou, J.B. Goodenough, J.-M. Lee, Superior oxygen electrocatalysis on nickel indium thiospinels for rechargeable Zn-air batteries, ACS Mater. Lett. 1 (2019) 123–131, https://doi.org/10.1021/acsmaterialslett.9b00093.

[59] G. Fu, X. Yan, Y. Chen, L. Xu, D. Sun, J.-M. Lee, Y. Tang, Boosting bifunctional oxygen electrocatalysis with 3D graphene aerogel-supported Ni/MnO particles, Adv. Mater. 30 (2018), 1704609, https://doi.org/10.1002/adma.201704609.

[60] J. Chen, C. Fan, X. Hu, C. Wang, Z. Huang, G. Fu, J.-M. Lee, Y. Tang, Hierarchically porous Co/CoxMy (M = P, N) as an efficient Mott–Schottky electrocatalyst for oxygen evolution in rechargeable Zn–Air batteries, Small 15 (2019), 1901518, https://doi.org/10.1002/smll.201901518.

[61] H. Wang, J. Li, K. Li, Y. Lin, J. Chen, L. Gao, V. Nicolosi, X. Xiao, J.-M. Lee, Transition metal nitrides for electrochemical energy applications, Chem. Soc. Rev. 50 (2021) 1354–1390, https://doi.org/10.1039/d0cs00415d.